# Aquatic Ecosystems Science Using an Imaging Spectrometer

Ronald Lockwood<sup>a</sup>, Charles M. Bachmann<sup>b</sup>, Michael Chrisp<sup>a</sup>, Corrie Smeaton<sup>a</sup>, Nima Pahlaven<sup>c</sup>, Eric Hochberg<sup>d</sup>, Marcos J. Montes<sup>e</sup>, Bo-Cai Gao<sup>e</sup>, Robert Frouin<sup>f</sup>, Anthony Vodacek<sup>b</sup>, Cedric Fichot<sup>g</sup>, Tom W. Bell<sup>h</sup>, Roy A. Armstrong<sup>i</sup>, Chunyan Li<sup>j</sup>, Laura Kennedy<sup>a</sup>, Steve Gillmer<sup>a</sup>, Linda Fuhrman<sup>a</sup>, Derrick Brouhard<sup>a</sup>, Jade Wang<sup>a</sup>, and Kurtis Thome<sup>k</sup>

<sup>a</sup>MIT Lincoln Laboratory, 244 Woods Street, Lexington, MA, USA <sup>b</sup>Rochester Institute of Technology, Chester F. Carlson Center for Imaging Science, Rochester, NY, USA

<sup>c</sup>Science Systems and Applications, NASA Goddard Space Flight Center, 8800 Greenbelt Road, Greenbelt, MD, USA

<sup>d</sup>Bermuda Institute of Ocean Sciences, 17 Biological Station, St. George's GE01, Bermuda <sup>e</sup>Remote Sensing Division, Naval Research Laboratory, Code 7231, 4555 Overlook Avenue, SW, Washington, DC, USA

<sup>f</sup>Scripps Institution of Oceanography, University of California, San Diego, 9500 Gilman Drive, La Jolla, CA, USA

gDepartment of Earth and Environment, Boston University, 685 Commonwealth Ave, Boston, MA, USA

<sup>h</sup>Woods Hole Oceanographic Institution, 266 Woods Hole Road, Woods Hole, MA, USA <sup>i</sup>Department of Marine Sciences, University of Puerto Rico, Mayaguez, P.O. Box 9000, Mayaguez, Puerto Rico

<sup>j</sup>Department of Oceanography and Coastal Sciences, Louisiana State University, 1002-Y Energy, Coast & Environment Building, Baton Rouge, LA, USA <sup>k</sup>NASA Goddard Space Flight Center, 8800 Greenbelt Road, Greenbelt, MD, USA

### ABSTRACT

The study of aquatic ecosystems is an important research area addressing diverse problems such as carbon sequestration in coastal margins and wetlands, kelp and seagrass studies, coral reefs, harmful algal blooms and hypoxia, and carbon cycling in this dynamic environment. The application of an imaging spectrometer to aquatic ecosystem study is particularly challenging due to low water-leaving radiance levels adjacent to the shore region with its higher values. The Committee on Earth Observation Satellites (CEOS) has established more stringent performance standards for the visible/near infrared wavelengths than are typically available in imaging spectrometer designs. We have recently developed a compact form imaging spectrometer, the Chrisp Compact VNIR/SWIR Imaging Spectrometer (CCVIS), that facilitates their modular usage with a wide field telescope without sacrificing performance. The CCVIS design and the operational concept have predicted performance that approaches the CEOS standards. The envisioned satellite implementation requires a pitchback maneuver where the imaging of the slit projected onto the surface is slowly scanned while recording focal plane array readouts at a higher rate thereby avoiding saturation over the land surface while obtaining a high signal-to-noise ratio over the water. The effective frame rate is determined by the time it takes to scan the projected slit one ground sample distance (GSD). This approach has the added benefit of measuring a range of angles during a single GSD acquisition, providing insight into the bidirectional reflectance distribution function (BRDF).

DISTRIBUTION STATEMENT A. Approved for public release. Distribution is unlimited.

Further author information: (Send correspondence to R.B.L. or C.M.B.) R.B.L.: E-mail: ronald.lockwood@ll.mit.edu, Telephone: 1 781 981 1803 C.M.B.: E-mail: Charles.Bachmann@rit.edu, Telephone: 1 585 475 7238

This material is based upon work supported by the Department of the Air Force under Air Force Contract No. FA8702-15-D-0001. Any opinions, findings, conclusions or recommendations expressed in this material are those of the author(s) and do not necessarily reflect the views of the Department of the Air Force.

©2023 Massachusetts Institute of Technology.

Delivered to the U.S. Government with Unlimited Rights, as defined in DFARS Part 252.227-7013 or 7014 (Feb 2014). Notwithstanding any copyright notice, U.S. Government rights in this work are defined by DFARS 252.227-7013 or DFARS 252.227-7014 as detailed above. Use of this work other than as specifically authorized by the U.S. Government may violate any copyrights that exist in this work.

**Keywords:** aquatic ecosystems, imaging spectroscopy, hyperspectral imaging

### 1. INTRODUCTION

Aquatic ecosystems are a vital resource that are relied upon for livelihoods, food, water, and safety. Currently 40% of the global population lives within 100 km of a coast, and this concentration is predicted to increase by 8–22% in the next 15 years. Aquatic ecosystems are under stress from climate change due to rising sea levels, temperature and increasing severity of episodic events such as storms and algal blooms. This combined with anthropogenic stressors such as pollution and eutrophication as well as encroachment of human development have brought many of these systems to potential tipping points. The increasing damage to and loss of these habitats comes at a high cost environmentally as well as economically.

Several space-based imaging spectrometers have been either deployed or are under development, however, none of these spectral imagers are specifically designed to address the challenges of coastal and inland water systems. These devices are based on dispersive spectrometers typically employing gratings that measure spectral radiance via pushbroom data acquisition where the slit projection onto the surface is advanced about one ground sample distance (GSD) during the time required for a single focal plane array (FPA) readout. The orbital kinematics of the satellite altitude and the signal-to-noise ratio (SNR) requirements are used to set the integration time (within FPA limitations) which also sets the GSD. A typical earth-viewing spectral remote sensing system such as the LandSat series or the future Surface Biology and Geology (SBG) system has a 30 m GSD which corresponds to a frame rate of about 250 Hz, which is well matched to the readout capability of the FPA technology. The predicted SNR for SBG is >300 for the 380-1750 nm spectral range (outside of the deep atmospheric absorption features) and is >100 for most of the 2000-2500 nm range.<sup>6</sup> This well-designed imaging spectrometer is ideally suited to meet the requirements specified in National Academies of Sciences, Engineering, and Medicine report Thriving on Our Changing Planet: A Decadal Strategy for Earth Observation from Space (referred to as the Decadal Survey).<sup>7</sup>

An imaging spectrometer specifically designed to address aquatic ecosystem science has different spectral and radiometric requirements. The primary source utilized to define the system is from the Committee on Earth Observations Satellites (CEOS) report Feasibility Study for an Aquatic Ecosystem Earch Observing System (referred to as the CEOS report). The CEOS report was developed by a panel of subject matter experts specifically focused on space-based remote sensing of aquatic ecosystems. The methodology establishing the recommendations is well documented in Gage and Dekker. Table 1 is a summary of the sensor requirements from the CEOS report. The spatial requirements are for the GSD. The spectral requirements are interpreted as the full width at half maximum  $\Delta\lambda$  of the individual instrumental profiles. The CEOS radiometric requirements are for imagery over dark water bodies with the radiometric performance metric being the noise equivalent spectral radiance (NE $\Delta$ L).

The CEOS requirements are limited to the 380–1000 nm range while an understanding of the water-shore interface zone requires measurements through the SWIR. Additionally, the SWIR bands improve the atmospheric compensation to yield more accurate water-leaving radiance and surface reflectance. Onshore measurements also require even higher SNR since the surface reflectance and the resulting at-aperture radiance are reduced as the soil wetness increases. We have chosen the Decadal Survey SNR requirements of  $\geq$ 400 (380–1100 nm) and  $\geq$ 250 (1100–2500 nm) as a threshold although the reflectance variability places a premium on high SNR.

Table 1. CEOS Requirements

Requirements	Values
Spatial	17 m baseline, 33 m threshold
Spectral	$380\text{-}730~\text{nm}$ - $\Delta\lambda$ : 5-8 nm $380\text{-}400~\text{nm}$ , $730\text{-}1000~\text{nm}$ - $\Delta\lambda$ : 15 nm with additional bands for atmospheric compensation (1130 nm, 1380 nm)
$\begin{array}{c} {\rm Radiance} \\ ({\rm mW/m^2sr/nm}) \end{array}$	100 (380-640 nm) 20 (640-1000 nm)
$\frac{\rm NE\Delta L}{\rm (mW/m^2sr/nm)}$	0.005 optimal 0.010 baseline
Temporal	As high as feasible

# 2. AQUATIC ECOSYSTEM SCIENCE

The state-of-the-art hyperspectral imaging system described here is designed for the particular challenges encountered in the coastal zone and its ecosystems. As noted earlier, such a system must have high SNR to contend with the low reflectance levels of the water column. The imaging system must also have good dynamic range to acquire imagery of suitable quality in the coastal margin where the dark water column and bright land surfaces are intermingled. In addition, the imaging system must have sufficient spectral resolution and band spacing to capture and distinguish critical spectral features important to each application. Many of these ecosystems have significant variability on small spatial scales also necessitating higher spatial resolution.

Water column hyperspectral imaging is only possible in the visible and near infrared (VNIR) portion of the spectrum, however, since 90% of at-sensor radiance over water comes from the atmosphere, the atmospheric correction of imagery over coastal waters is particularly challenging and necessitates spectral information from the short-wave infrared (SWIR) to produce the highest quality products. Compared with ocean color applications, the importance of SWIR bands for atmospheric correction is particularly critical for coastal zone imaging due to the increased variability of aerosols in this region, the highly absorbing nature of many of the aerosols from anthropogenic sources in this region, and, in the NIR in coastal waters, the increased response, which limits the effectiveness of techniques based solely on the NIR for modeling aerosol species and concentration. The inclusion of a SWIR spectral range also improves the quality of retrieved products in the coastal margin, related to, for example, soil organic carbon in coastal wetlands as well as above-ground biomass.

The imaging spectrometer design described here can play a significant role in a wide variety of coastal zone ecosystems. These include coastal wetlands and margins, corals, seagrasses and kelp, carbon cycling and sequestration in these systems, harmful algal blooms and hypoxia, as well as pollution, eutrophication, and water quality in coastal waters. The advantages of a high-SNR system that also includes SWIR bands as well as higher GSD could be used to address the goals described below in these critical coastal zone ecosystems. We conclude this section with a discussion of the specific benefits of including SWIR bands for atmospheric correction even over water scenes. This specific feature will greatly enhance the quality of the hyperspectral imagery obtained for all of the aquatic ecosystem science applications described below.

## 2.1 Coastal Margins and "Blue Carbon"

Although significant emphasis has historically been placed on forest ecosystems as a primary mechanism of carbon sequestration, estimates of contributions from coastal ecosystems, so-called "Blue Carbon", are comparable to those of forest ecosystems globally. These systems include coastal wetlands, seagrasses, and mangroves which combined sequester carbon at estimated rates ranging between 84-233 Teragrams (Tg) C yr<sup>-1</sup> while forest ecosystems (temperate, topical, and boreal combined) contribute an estimated 180.8 Tg C  $yr^{-1}$ . One of the key challenges is that current estimates of "Blue Carbon" have large error bars as just noted. The CCVIS hyperspectral imaging system will directly address this issue, providing invaluable information to carbon cycle models as well as to natural resources managers. Below we briefly describe different specific ecosystem applications that CCVIS hyperspectral imagery can help to improve.

#### 2.2 Wetlands

Coastal wetlands are an important contributor to global carbon with estimates ranging from 5-87 Tg C yr<sup>-1</sup>.<sup>12</sup>, <sup>14</sup> Wetlands provide important ecosystem services and serve as functional barriers protecting coastal communities from severe storm events. Sea-level rise has led to significant marsh dieback in recent decades with historical losses in the last century estimated to be as high as 25% globally. <sup>12</sup> At the same time, coastal wetlands have experienced significant stress due to sea-level rise, encroachment, and nutrient loading, and many of these signs of salt marsh stress are detectable in hyperspectral data. <sup>15</sup> Wetland systems store carbon in both the above-ground biomass as well as the sediments, however, the large variance in estimates of global carbon sequestration in coastal wetlands reflects several inherent challenges. One is that variations in species between low- and high-marsh vegetation types can change rapidly with elevation since species composition varies with local micro-topography, contributing to difficulties in accurate estimates, especially when these variations are sub-pixel. Historical satellite imagery, with poorer spatial resolution, spectral coverage, and SNR contributed to the limited accuracies just cited.

Soil organic carbon estimates are more complicated because in tidally driven systems like coastal wetlands, sediments may be exposed at low tide but are often submerged or heavily inundated at high tide. Wind stress during severe weather can also inundate or drain wetlands, e.g. in coastal Louisiana, a microtidal regime, <sup>16</sup> although this same process may occur on larger times scales due to longer duration and less regular particle excursion, especially in diurnal tide regions.<sup>17</sup> In general, coastal wetland products derived from imagery are more error-prone and complicated precisely because of the variable amount of water within the system<sup>18, 19</sup> during the diurnal cycle, leading to large temporal variations daily in spectral reflectance at any given scene location. These issues particularly effect vegetation indices relying on just a few spectral bands, especially those involving the NIR, where inundation has a dramatic spectral effect. 19 Improvements in salt marsh biomass retrievals and species map accuracy depend on properly accounting for the variable amount of water in the mixture. Retrievals of above-ground biomass in coastal wetland systems have frequently used spectral vegetation indices and/or regression techniques to identify bands highly correlated with above-ground biomass. <sup>20,21</sup> Other methods include clustering and vector quantization approaches, as well as machine learning.<sup>22,23</sup> Another particularly promising approach uses radiative transfer models traditionally applied to other vegetation canopy types, such as those found in forestry and agriculture; these models have now been used successfully to predict above-ground salt marsh biomass.<sup>24</sup>

Because of the inherent challenges just described, accurately quantifying carbon storage in wetland systems requires the features described in the CCVIS hyperspectral imaging system described in this work. The high SNR of CCVIS in the VNIR makes it an excellent choice for aquatic applications such as wetland environments in the coastal margin; CCVIS coverage of both VNIR and SWIR spectral bands can provide improved atmospheric correction of imagery<sup>11</sup> leading to greater accuracy in all retrieved products, and the inclusion of SWIR bands with higher SNR means that above-ground biomass<sup>18</sup> as well as soil organic carbon (SOC) retrievals<sup>25</sup> will be much improved.<sup>26</sup>

#### 2.3 Kelps and Seagrasses

Surface canopy-forming kelps are marine foundation species dominating coastal waters in temperate regions worldwide. Kelps, such as giant kelp ( $Macrocystis\ pyrifera$ ) and bull kelp ( $Nereocystis\ luetkeana$ ), have high rates of net primary production<sup>27</sup> and create complex, three-dimensional structure throughout the water column, <sup>28</sup> providing food and habitat for many ecologically and economically important species.

Canopy-forming kelps have high growth rates and dynamic populations, as the abundance of these species fluctuates rapidly and is sensitive to several environmental drivers.<sup>29</sup> While multiple variables have been linked to changes in kelp abundance, kelp forest response to changing environmental conditions and anthropogenic stressors exhibits high spatial variability.<sup>30</sup> Over the past decade, increases in frequency, magnitude, and duration of marine heat waves has led to deleterious effects on global kelp forest systems. In Australia, extreme warming has been linked to major declines in kelp forest ecosystems.<sup>31</sup> From 2014 to 2016 an unprecedented marine heatwave led to large declines in kelp abundance across California and Baja California, Mexico when ocean temperatures crossed the physiological threshold of giant kelp.<sup>32</sup> While many kelp populations in southern California and Baja California recovered within a few years, bull kelp forests in northern California displayed little resilience

and were replaced with large-scale purple sea urchin barrens,  $^{33}$  leading to closures of important fisheries such as red abalone and red sea urchin.  $^{34}$ 

Remote sensing is a powerful tool for monitoring canopy-forming kelps and repeat satellite imagery has enabled regular monitoring of canopy area and biomass across multiple space and time scales. The Landsat satellite program has been particularly valuable for kelp monitoring on regional to global scales, as it provides imagery with continuous global coverage at a 30 m resolution since 1982. This dataset has been used to detect long-term trends in kelp abundance and put changes due to marine heatwaves in a broader historical context. The floating surface canopy reflects NIR light at much higher magnitudes than the surrounding sea water allowing legacy multispectral sensors to accurately measure canopy dynamics. Over the past several years, the availability of repeat hyperspectral imagery from airborne campaigns has led to several advances in the measurement of canopy physiological condition. Physiological condition is estimated through the measurement of the chlorophyll to carbon ratio (Chl:C) and is linked to changes in the external light and temperature/nutrient environment and declines predictably with age. The combination of Chl:C and biomass estimates will also be key for the assessment of net primary production.

The ground sample distance of the CCVIS hyperspectral imaging system described in this work is well suited for the measurement of kelp canopy as most forests will be comprised of many pixels, making CCVIS an ideal choice for the visualization of local scale patterns in canopy biomass and physiological condition. Additionally, the spectral coverage, resolution, and SNR will be adequate for the repeat estimation of physiological condition as the AVIRIS-based algorithm for that purpose has been validated with *in situ* measurements. With the increased SNR, several additional algorithms could be developed such as the fucoxanthin to chlorophyll ratio, an indicator of physiological stress.

Like canopy-forming kelps, seagrasses play an important role providing structure for shallow marine ecosystems with the added benefit of providing carbon storage within adjacent sediments, sediment stabilization, and shoreline protection.<sup>39</sup> However, despite their importance, seagrass is threatened by a variety of environmental and anthropogenic stressors, such as high temperatures, declining habitat, and coastal development.<sup>40</sup> Several studies have investigated the use of hyperspectral imagery for seagrass. Hill and others<sup>41</sup> used airborne hyperspectral data to evaluate the areal extent and leaf area index of seagrass meadows in the optically complex waters of Saint Joseph's Bay, Florida. Phinn and others<sup>42</sup> evaluated both hyperspectral and multispectral imagery and found that airborne hyperspectral data produced the highest overall accuracies for both species type and aboveground biomass. Both studies showed that decreased ground sample distance led to underestimates of biomass. Additionally, water column optical modeling will be essential for reducing ancillary in situ data collection and facilitating the use of hyperspectral imagery for routine monitoring of seagrass. The spectral coverage, resolution, and SNR of the CCVIS hyperspectral imaging system described here will be sufficient for shallow water optical modeling and may allow for more accurate estimates of seagrass areal extent and net primary production.

### 2.4 Carbon Cycling

Organic carbon (OC) is a major and dynamic pool of reduced carbon fulfilling important ecological and biogeochemical functions in aquatic systems. Throughout the aquatic land-ocean continuum, organic carbon is produced, transformed, and mineralized to CO<sub>2</sub> by a combination of biotic and abiotic processes, and transported laterally and vertically by physical processes. On land, terrigenous OC is mobilized from soils and transported through streams, rivers, wetlands, and lakes before reaching the ocean. These inland-water systems are major reactors that extensively process and mineralize terrigenous OC and contribute globally significant fluxes of CO<sub>2</sub> to the atmosphere. Part of that OC eventually reaches the ocean, and rivers deliver about 0.4 Pg of terrigenous OC to the coastal ocean each year. Tidal salt marshes are also significant sources of OC to estuaries. Upon entering the ocean, most of this exported particulate OC sinks and a fraction gets buried and sequestered in the sediment. A large but variable fraction of the dissolved OC gets further processed and mineralized in the coastal ocean where it sustains microbes and influences the metabolic balance of aquatic ecosystems and their role in CO<sub>2</sub> exchange. Primary production in aquatic systems also generates autochthonous particulate and dissolved OC, further complicating the cycling of organic carbon. Sp. Evidence indicates that the stocks, fluxes, and functions of OC in aquatic systems are vulnerable to human activities and climate-driven perturbations. Land-cover disturbance, warming and thawing of soils, changing hydrology,

and degradation of wetlands are all environmental perturbations influencing the mobilization and processing of terrigenous OC waters and its influx to the coastal ocean. $^{61,65}$  Increasingly frequent extreme events such as floods and hurricanes lead to major pulses of export of terrigenous OC and nutrients fueling the autochthonous production of OC. $^{66}$ 

Warming, acidification, enhanced water-column stratification, and changing ocean circulation can also affect the transport, production and cycling of OC and exert feedback on its functions and climate. The question of how OC stocks, fluxes and transformations are currently changing remains largely open, but a detailed understanding of current and future changes in OC cycling requires the ability to monitor OC stocks and fluxes across different environmental conditions and spatiotemporal scales, and to assimilate these data into realistic models.

Satellite remote sensing represents one of our best assets to monitor OC in aquatic systems and to inform models to document and understand change in the OC cycle. Monitoring the dynamics of OC can be facilitated in large parts of the ocean by existing multispectral ocean-color sensors and by upcoming sensors acquiring data on scales of 300-m to 1-km on daily or sub-daily timescales.<sup>67</sup> However, the capabilities of these assets become very limiting when monitoring OC in the nearshore coastal ocean, at the land-ocean interface (e.g., estuaries and coastal wetlands) and in inland waters, where waters and atmospheric conditions are optically complex and make the accurate retrieval of IOPs and derived OC products challenging, sharp gradients in OC occur over spatial scales of tens of meters and require high-spatial (e.g., < 50m) resolution imagery, and currents and tides drive OC dynamics on short timescales.<sup>68-71</sup> Furthermore, these waters are often subject to extreme events (e.g., storms, snow melt, harmful algal blooms) that have drastic impacts on OC cycling<sup>72,73</sup> but are episodic and very challenging to capture adequately.

The CCVIS will fill an existing gap in our capability to monitor OC dynamics in these critical aquatic systems which are within the direct influence of human activities and climate-driven changes. Its unique combination of high SNR, hyperspectral capabilities, extended spectral range, high spatial resolution, and possibility of targeted frequent acquisition will better capture the variability of OC in these optically complex, dynamic, and heterogenous aquatic systems. Specifically, the high SNR, hyperspectral, and SWIR capabilities will facilitate the accurate retrieval of IOPs (e.g., CDOM absorption coefficient spectra, particulate absorption coefficient spectra, particulate backscattering coefficients spectra) used as optical proxies for dissolved and particulate organic carbon concentration in the optically complex settings typically encountered in or near terrestrial environments, or where bottom reflectance is significant and variable. Hyperspectral measurements of reflectance are preferrable in optically complex waters as they provide more detailed spectral information to constrain the independent optical variabilities of the water constituents. Furthermore, the combination of high spatial resolution and the possibility of frequent acquisition of imagery over a specific target will facilitate capturing OC dynamics in tidally influenced systems and before, during, and after episodic events. The CCVIS will also facilitate the retrieval of key IOPs and other optical variables (e.g., incident irradiance) needed for modeling rates of primary production and photochemical processing <sup>74</sup>.<sup>75</sup>

#### 2.5 Coral Reefs

Coral reefs are distributed throughout the world's tropical oceans, directly occupying an estimated area of  $250,000-600,000 \text{ km}^2$ . These values correspond to  $\sim 0.05-0.15\%$  of the global ocean area, respectively, and about 5-15% of the shallow sea areas within 0-30 m depth. Coral reefs have ecological and economic importance that is disproportionately large relative to their areal extent. The global economic valuation of the direct and indirect use of coral reefs has been estimated near \$10 trillion annually. While the accuracy of this dollar amount is debatable, it is certain that coral reefs are important to the cultural and economic lives of hundreds of millions of people around the world, providing food for innumerable small subsistence economies, shoreline protection, superlative recreational resources, and biological storehouses for the biotechnology industry.

The concern for reef futures—and indeed documented ongoing coral loss at several reefs—has motivated assessment and monitoring efforts globally. Local and regional surveys have disparate objectives and often utilize different methods, but they invariably share a common metric for reef status: benthic cover, or the relative abundances of corals, various algae, and sediment, which are fundamental reef benthic types. Reference types are cover, in particular, is the primary focus in assessment and prediction of reef trends.

To the present, satellite sensors have been incapable of assessing global coral reef status, because they lack the necessary spectral resolution to discriminate key benthic types: coral, algae, and sand. Numerous case studies have demonstrated the ability for multispectral sensors (either moderate or high spatial resolution, e.g., Landsat or WorldView, respectively) to produce reasonably accurate maps of reef "habitats," which has led to efforts such as the Millennium Coral Reef Mapping Project and the Allen Coral Atlas. These projects have generated reasonable depictions of reef location and ecological zonation within reefs, but owing to their spectral limitations, their map products fail to answer the fundamentally important questions to reef ecology: how much coral is there and what is the (statistical) relationship between benthic community structure and environmental forcings?

Imaging spectrometry (i.e., hyperspectral imaging) is required to discriminate between reef benthic types, and thus quantify benthic cover. <sup>85</sup> This is the basis for the recent NASA EVS-2 mission COral Reef Airborne Laboratory (CORAL), which in 2016–2017 successfully mapped 10,000 km<sup>2</sup> of reef area across the Great Barrier Reef, Hawaii, Mariana Islands, Palau, and Florida. Unfortunately, there are no global imaging spectroscopy data sets; airborne missions like CORAL and spaceborne imagers such as DESIS have small acquisition footprints and insufficient SNR. The NASA SBG mission is expected to provide global coverage of spectral imagery, but not until late in the decade.

The system that we describe here has several advantages for coral reef systems. A nominal orbit and pointing capability would afford a probability  $\geq 0.5$  for at least one engagement in a year with 58% of the world's reef area at a cloud fraction  $\leq 0.2$ . For two years on orbit, the number increases to 85% of the world's reef area engaged at least once and 62% engaged twice. These areas represent a 30-fold increase in sample size over CORAL and a 5,000-fold increase over in-water surveys. Furthermore, the spectral coverage, resolution, and SNR, as well as the ground sample distance, of the sensor are ideally suited to the task of coral reef retrievals. The necessary algorithms have already been developed for CORAL, <sup>86</sup> and further refinements are ongoing. Level-2 (and -3) map products can be generated rapidly for input to reef science analyses.

# 2.6 Harmful Algal Blooms and Hypoxia

Harmful algal bloom (HAB) and hypoxia episodes affect coastal waters across the US and include both inland waters such as the Great Lakes as well as coastal ocean waters. HABs pose considerable safety concerns due to the potential for associated harmful neurotoxins,<sup>87</sup> directly threatening health of residents in coastal communities. HABs affect drinking water, fisheries, marinas, and other coastal businesses. A study in 2000 estimated that HABs cost the US economy alone between \$34M-\$82M annually,<sup>88</sup> which in today's dollars is equivalent to \$60M-\$228M annually.<sup>89</sup> Eutrophication that contributes to the development of HABs in summer months also promotes the development of hypoxia in coastal waters,<sup>90</sup> which can have a devastating impact on commercial fishing.<sup>91–94</sup> The hypoxic zone off the Louisiana coast is the second largest human-caused coastal hypoxic area in the global ocean. Such conditions have been found year round but are mostly seasonal especially in summer, for example, on the Gulf Coast<sup>95, 96</sup> where the Gulf of Mexico Coastal Ocean Observing System (GCOOS) has been charged with the task of monitoring and quantifying the extent of hypoxic "dead zones".<sup>97</sup>

The area of the hypoxic zone depends on river discharge, nutrient input, and stratification which is highly influenced by solar radiation and wind stress and thus highly variable. <sup>98–100</sup> While remote sensing systems are now widely incorporated in HAB monitoring and forecasting, most of these resources are multi-spectral systems that, while providing good spatial coverage, do not have the spectral resolution to detect the earliest stages of HAB evolution and are less accurate for mapping purposes than what could be achieved by a hyperspectral imaging system that also has sufficient spatial resolution. Hypoxic zones have been studied using MODIS imagery (36 spectral bands, visible through thermal), and indicators of the presence of bio-optical signatures typical of hypoxic zones have been identified. <sup>101</sup> However, the large ground sample distance (GSD) does not provide fine detail of the spatial distribution of hypoxic events or of HAB epsiodes. <sup>102</sup>

The cyanobacteria responsible for HABs have unique optical properties from accessory pigments such as phycocyanin, phycocyathin, and fucoxanthin  $^{103,\,104}$  that lead to specific signals detectable with remote sensing.  $^{105-108}$  Phycocyanin, used as the basis of many detection and mapping algorithms, has absorption features that are spectrally close to those of chlorophyll-a, -b, and -c, with the closest of these features being within  $20\,nm$  of a chlorophyll absorption feature.  $^{103}$  This emphasizes the importance of both narrow band spacing and

spectral resolution as well as excellent SNR, which are characteristics of the CCVIS hyperspectral imaging system described in this work. The band spacing ( $\leq 10 \, nm$ ) of the CCVIS hyperspectral imaging system will fall well within the requirements to separate pigments such as phycocyanin from background chlorophyll signatures

Since 2011, there has been a sudden increase in Sargassum biomass in the tropical Atlantic and Caribbean Sea and consequently, massive accumulations of Sargassum have been reported in the coasts of the Eastern and Western Caribbean and Florida. Massive Sargassum beachings are now considered HABs<sup>111</sup> due to significant and persistent light attenuation and habitat displacement of benthic ecosystems such as coral reefs and seagrass beds. Inpacts in coastal environments from Sargassum accumulation include fish mortality, altered coastal and wetland biochemistry, release of toxic products due to decomposition, and beach accumulations that impact sea turtles and other important species in coastal and marine reserves.

Satellite remote sensing data have been used to identify and monitor Sargassum distribution throughout the Greater Caribbean and Atlantic regions using a simple ocean color index, namely the Floating Algae Index (FAI). Remote detection of pelagic Sargassum is often hindered by its spectral similarity to other floating materials and by inadequate spatial resolution. Hyperspectral data, with improved spectral and spatial resolution, is required to enhance current capabilities. Coastal Sargassum accumulations have been documented to produce fish mortality and "black water" has been observed due to "leaching" from the Sargassum at various stages of decomposition. Spectral discrimination of Sargassum decomposition stage at coastal accumulation sites will enable us to determine its potential impact on mangroves and benthic shallow communities as well as quantify the area of impact and magnitude of the leaching "black water".

In addition to chlorophyll, HAB accessory pigments must be detected and quantified amidst a complex background of contributions from water column constituents. Methods to detect and quantify HABs include semi-empirical models, <sup>103</sup> band ratios and indices, <sup>107,117-119</sup> as well as radiative transfer models. <sup>120,121</sup> Band indices are often chosen for multi-spectral satellite retrievals due to the limited number of available spectral bands with wider band-pass. The radiative transfer model approach <sup>122</sup> has typically used existing software tools, such as Hydrolight, <sup>123</sup> which incorporates bio-optical components and additional inputs such as user-based reference spectra from, for example, bottom reflectance measurements. In such approaches, a hyperspectral look—up table (LUT) is produced from the forward radiative transfer model, linking predicted spectra to a specific combination of in-water component concentrations (chlorophyll, phycocyanin, color-dissolved organic matter (CDOM), total suspended sediment (TSS), phytoplankton), the bottom reflectance, and water depth. <sup>120,121,124-126</sup> By constructing a comprehensive LUT using a radiative transfer forward model and matching hyperspectral imagery pixels to the LUT, water constituent concentrations are retrieved. Our past research, for example, has used radiative transfer model inversion to retrieve in-water optical properties from both multi-spectral and hyperspectral imagery, <sup>120,121,125,126</sup> particularly focused on retrieval of phycocyanin concentration for HAB detection in both Landsat multi-spectral imagery (MSI) and unmanned aerial system (UAS) hyperspectral imagery. <sup>121</sup>

### 2.7 Atmospheric Correction of Imagery for Coastal Zone Applications

Atmospheric correction only removes atmospheric scattering and absorbing effects from calibrated data. Other corrections, such as mitigating ocean surface glint and the effects of thin cirrus clouds, can also be performed at this processing pipeline stage. CCVIS VNIR and SWIR coverage and high SNR allow for all these corrections. Due to high water absorption in the SWIR (compared to the NIR), 127 no light is scattered from below the surface. This allows SWIR based glint and/or atmospheric correction. Likewise, narrow channels located within the 1380- and 1880-nm atmospheric water vapor band centers are very effective in detecting thin cirrus clouds. 128

For atmospheric correction of the VNIR/SWIR imagery, we have developed a method designed for hyperspectral imagery having both NIR and SWIR spectral bands.<sup>129</sup> Lookup tables for 14 wavelengths between 390 and 2500 nm in atmospheric "window" regions, sets of aerosol models, optical depths, solar and view angles, and surface wind speeds have been generated. Aerosol models, similar to those used previously, <sup>130</sup> are used during our table generation. Our algorithm uses a sophisticated line-by-line based atmospheric transmittance code to calculate contiguous atmospheric gaseous transmittance spectra.

Alternative atmospheric correction approaches also address absorbing aerosols, thin clouds, Sun glint, optically complex and shallow waters, and adjacency effects. One approach <sup>131, 132</sup> decomposes top of atmosphere

(TOA) CCVIS data, after correction of gaseous absorption, into principal components (PCs), selects PCs most sensitive to water signal, and combines selected PCs to retrieve PCs of water reflectance, to reconstruct water reflectance. Non-parametric regression techniques then are used to map the various PCs. Eigenvectors of TOA and water body reflectance are determined using a comprehensive ensemble of expected situations (geophysical, geometric) generated from ARTDECO<sup>133</sup> radiative transfer simulations. Water bidirectional reflectance is then computed using Hydrolight. Benthic reflectance is a weighted sum of reflectances of basic substrates (e.g., coral, seagrass, sand). Adjacency effects are incorporated using models for typical surfaces (e.g., vegetation, bare soil sand, ice) according to Santer and Schmechtig. In the ensemble, expected noise in the Level 1b imagery then is modeled as the sum of spectrally uncorrelated and correlated Gaussian noise of varied amplitude.

To map the PCs, the TOA signal in strong gaseous absorption bands is not used because scattering and absorption processes cannot be easily decoupled for some absorbers (e.g., water vapor). But it is still possible to associate PCs of the measured signal outside absorbing bands to the water reflectance PCs defined on a different base, allowing an estimate of the water reflectance inside the absorbing bands. This provides continuous water reflectance over the entire CCVIS spectral range.

### 3. IMAGING SPECTROMETER DESIGN AND PERFORMANCE

The ideal imaging spectrometer design for aquatic ecosystems is one with a wide field, for broad area coverage, in addition to meeting the requirements presented in Table 1. The spectral and radiometric requirements drive the design of the spectrometer with the shape and spacing of the instrumental profiles, the lowest possible F-number and the largest detector elements to produce the high étendue required for the NE $\Delta$ L performance. In addition the spectrometer design optimizes the optical transmission over the spectral range through the glass choice and the grating efficiency. The telescope design supports the field of view (FOV), which can be large for a modular implementation.

An imaging spectrometer consists of a telescope, a spectrometer or multiple spectrometer modules, a FPA for each module, and the associated electronics. The SNR or NE $\Delta$ L are partially determined by the product of the étendue U, the geometric factor that determines the amount of flux that an instrument accepts, and the spectral transmission  $\tau(\lambda)$ , known as the luminosity  $\mathcal{L}$  in instrumental spectroscopy, and given by

$$\mathcal{L}(\lambda) = \tau(\lambda)U = \tau(\lambda)\frac{A_d\pi}{4N^2} \tag{1}$$

where  $A_d$  is the area of a detector element and N is the F-number. <sup>136</sup> In the case of a spectrometer that employs refractive materials, the design will optimize the optical glass transmission over the full spectral range and the multi-blaze grating will be designed to provide the best performance for the particular problem to be addressed. For a typical imaging spectrometer that is employed for land viewing, the grating efficiency will be biased to the longer wavelengths to improve the SNR performance where the radiance is low due to the decline in the solar Planck function. The étendue is maximized by reducing the F-number as much as possible. For example, a Dyson form such as Compact Wide Swath Imaging Spectrometer (CWIS) is F/1.8 and will have almost twice the étendue for equivalent detector areas when compared to an F/2.5 design. <sup>137</sup> In addition, stringent aberration control is required to produce high quality data products. <sup>138</sup> State-of-the-art imaging spectrometers meet this spatial-spectral uniformity requirement in both design and implementation.

Figure 1 illustrates the Chrisp Compact VNIR/SWIR Imaging Spectrometer (CCVIS) optical form that is comprised of a slit, a catadioptric lens, an immersed grating, and a focal plane array. The spectral range is 380–2500 nm with 5 nm spacing between adjacent instrumental profiles. The catadioptric lens has aspheric refractive elements with a spherical reflective back surface. The result is a compact spectrometer with the volume of the optical form being about 390 cm<sup>3</sup>. This is about an order of magnitude smaller than the similarly performing CWIS Dyson form. The blazed grating is designed to have higher optical efficiency at the short wavelengths ( $\lambda < 750$  nm) where the water-leaving radiance is low and relatively flat performance at the longer wavelengths. An advantage of the CCVIS is its manufacturability due to both the catadioptric lens comprised of centered optical elements and the flat grating, which is manufactured using gray-scale lithography. Note that the CCVIS will only accommodate a single FPA that supports the full 380–2500 nm range.

The CEOS radiometric requirements motivated the modification of the original CCVIS design for increased étendue in order to maximize the SNR. The CCVIS optical form is F/2.5 and cannot be made significantly faster so the pixel pitch was increased from 18  $\mu$ m in the original design to 36  $\mu$ m with the étendue increased by a factor of four. The number of detector elements for each CCVIS is 1500 spatial  $\times$  425 spectral samples producing a field of  $5.4 \times 1.53$  cm<sup>2</sup>. There are a variety of state-of-the-art arrays that are available to meet this spectral range requirement with different pixel pitches and numbers of detector elements offering implementation flexibility.<sup>141</sup> The high luminosity required for aquatic ecosystem science motivates increasing the size of the detector elements. The approach taken here is to utilize the Teledyne GeoSnap/CHROMA-D architecture and produce a new FPA with 36  $\mu$ m pixels without the reduction in SNR that would result in 2  $\times$  2 binning after data readout. A CCVIS prototype is currently being matured to TRL-6.

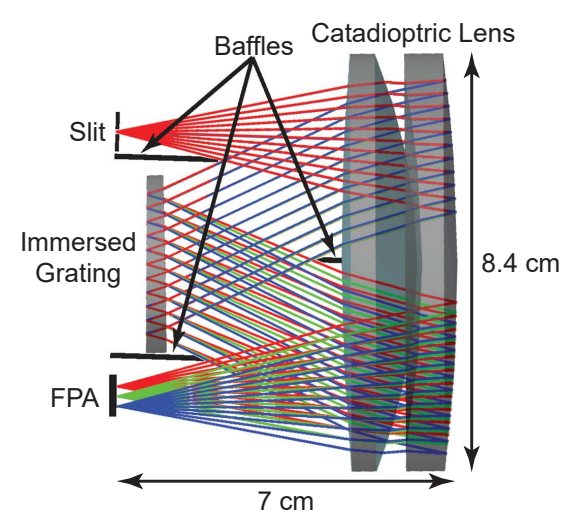


Figure 1. Chrisp Compact VNIR/SWIR Imaging Spectrometer

## 3.1 Radiometric Performance

The CEOS radiometric requirements are predicted based on a sensor model with the SNR and the NE $\Delta$ L utilized as metrics. However, the instrument performance is insufficient to meet the CEOS requirement, which is then addressed through a concept of operations employing a satellite pitch back maneuver. The model includes the signal expressed as the number of electrons recorded due to the at-aperture radiance, the background signal due to self-emission from the optical elements and the housing, and the dark signal due to the detector. The noise includes the shot noise due to all sources of photons, the dark current noise, the quantization noise, and the read noise from the focal plane array, however, the 1/f noise is neglected.

The radiometric modeling that results in estimates for the SNR and the NE $\Delta$ L is, for a particular spectral sample, based on the measurement equation given by

$$S(\lambda_c) = \frac{Ut_{int}}{hc} \int [L(\lambda)\tau(\lambda)\eta(\lambda)]\lambda P(\lambda_c - \lambda)d\lambda, \tag{2}$$

where U is the étendue,  $t_{int}$  is the integration time for one frame acquisition, h is Planck's constant, c is the speed of light,  $L(\lambda)$  is the spectral radiance,  $\tau(\lambda)$  is the system optical efficiency,  $\eta(\lambda)$  is the quantum efficiency of the HgCdTe detector, and  $P(\lambda_c - \lambda)$  is the instrumental profile for a spectral channel centered at  $\lambda_c$ . Equation (2) is applied to both the at-aperture spectral radiance and the self emission from the telescope, calculated using its reflectivity and temperature, that is dispersed by the spectrometer. It is modified in order to model the self emission from the optical elements that are optically downstream from the slit.

The CEOS reference radiance is listed in Table 1. The Decadal Survey reference radiance utilizes a flat, 25% Lambertian reflectance with the at-aperture spectral radiance generated with MODTRAN®5 using a midlatitude summer model with the default values, which agrees with the spectral radiance presented in Green et

al,  $2022.^6$  The spectral requirements are 380-2500 nm with a band spacing of  $\leq 10$  nm, which is lower spectral resolution than the CEOS requirements. The reference radiances are shown in Figure 2 with the Decadal Survey spectral radiance band averaged to the CCVIS instrumental profiles.

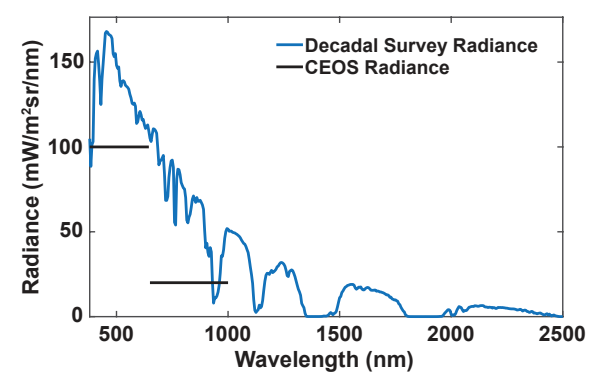


Figure 2. Decadal Survey and CEOS reference radiances.

The noise is dominated by the shot noise from the at-aperture radiance with a small contribution from sensor self emission. The dark current is from Teledyne Imaging Systems<sup>141</sup> and is scaled from an 18  $\mu$ m pixel to a 36  $\mu$ m pixel based on the ratio of the areas, with the noise calculated assuming Poisson statistics. The 400 electron read noise is from the Teledyne GeoSnap-18 fact sheet.<sup>142</sup> The quantization noise is calculated using

$$N_Q = \frac{w}{2^m \sqrt{12}} \tag{3}$$

where the well depth w is  $2.6 \times 10^6$  electrons, again taken from the GeoSnap-18 fact sheet, and m is the 14 bit analog to digital conversion. The noise terms are assumed to be independent and are combined using the square root of the sum of the squares of the errors.

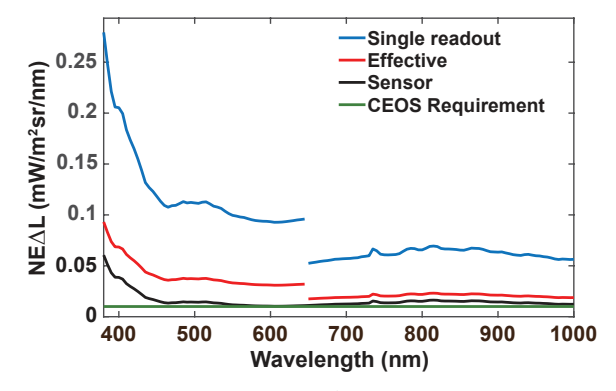


Figure 3. CEOS NE $\Delta$ L performance.

The effective NE $\Delta$ L in Figure 3 is produced by slowly scanning the projection of the slit across the surface and acquiring several FPA readouts as the slit projection advances one GSD during the effective integration time  $t_{eff}$ . The signal  $S_1$  from each acquisition is co-added to increase the total signal. The effective noise for  $n_{ro}$  readouts is

$$N_{eff} = \sqrt{n_{ro}} N_1 \tag{4}$$

where  $N_1$  is the single readout noise and the effective SNR is

$$SNR_{eff} = \frac{n_{ro}S_1}{N_{eff}} = \sqrt{n_{ro}}\frac{S_1}{N_1}.$$
 (5)

The number of readouts is the ratio of the effective integration time to the native integration time of the FPA. The NE $\Delta$ L is then the ratio of the band-averaged radiance to the SNR. Figure 3 also includes the sensor NE $\Delta$ L that is calculated from the radiometric resolution of the CCVIS. This is based on the at-aperture radiance that would be required to just fill the well of a particular spatial-spectral pixel. The noise in this case is due to dark current, quantization, read noise, and shot noise from sensor self-emission. Note that this depends on the optical and quantum efficiencies at a particular  $\lambda_c$ , providing the spectral variation.

Figure 4 shows the performance model SNR prediction corresponding to the CEOS and Decadal Survey radiance values from Figure 2 with the CEOS values shown as a reference. The figure also shows the Decadal Survey SNR requirements. The reference radiances meet the Decadal Survey requirements from 380 nm to 2400 nm with the exception of the atmospheric water absorption features.

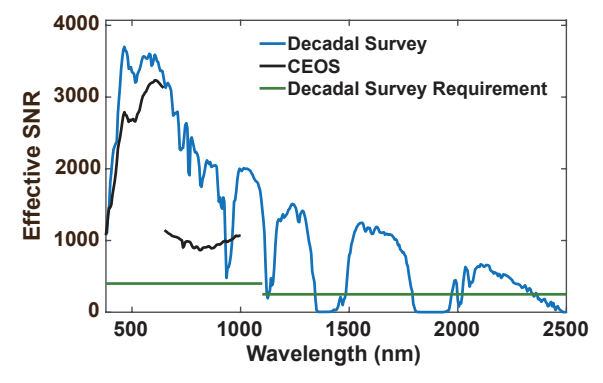


Figure 4. CEOS and Decadal Survey SNR performance.

The data aggregation method produces very high SNR values for an imaging spectrometer operating from space. However, the CEOS requirement is extremely challenging for any imaging spectrometer that employs a grating, which is a fundamentally inefficient optical element. Even a single-blaze grating that has high efficiency at the blaze wavelength will fall rapidly at shorter and longer wavelengths making it difficult to meet the 0.010 mW/m<sup>2</sup>sr/nm threshold over the full spectral range. The sensor NE $\Delta$ L would be improved by lowering the FPA read noise. For example, if the read noise were cut in half from 400 to 200 electrons, the sensor NE $\Delta$ L would go from 0.010 mW/m<sup>2</sup>sr/nm to 0.005 mW/m<sup>2</sup>sr/nm at 600 nm.

### 4. AREA COVERAGE

One of the strengths of the CCVIS is that it can be deployed as modules enabling wide field imaging spectrometers. The CEOS spatial sampling requirement has a 17 m baseline and a 33 m threshold. These values are used to design the pitchback maneuver with the initial along track nadir GSD being 33 m with the satellite pointing the sensor in the forward direction. As the satellite passes over the viewed area, the imaging spectrometer is rotated to pushbroom the slit along the surface with the 17 m GSD corresponding to nadir viewing and again reaching the 33 m GSD at the end of the swath. This produces a bow tie shaped swath for the viewed geometry. From the maneuver model and a 450 km low earth orbit deployment of the imaging spectrometer, there are 1168 along-track samples at the effective frame rate which produces an area coverage of 2272 km² for one swath acquisition using four CCVIS modules each with 1500 cross track spatial samples.

### 5. BRDF BENEFITS

Angular scattering measurements of the bi-directional reflectance distribution function (BRDF) provide significant information that can be useful in inverting surface properties in both the land and water and are complementary to that which the spectral domain provides. This principle was, for example, at the heart of NASA systems such as the Multi-Angle Imaging Spectroradiometer (MISR), designed to examine the properties of clouds, atmospheric constituents, and Earth's surface from multiple viewing geometries. <sup>143–149</sup> In particular, a multi-angular inversion approach has also been used with MISR for modeling water inherent optical properties

(IOPs) using radiative transfer models.<sup>150</sup> In general, multi-angular data provides access to directional scattering information which can constrain radiative transfer models to improve retrievals of biophysical or geophysical properties.<sup>151,152</sup> An extended pitchback maneuver over a large angular range would provide an unprecedented opportunity to examine the spectral BRDF to achieve these goals over coastal zone waters and margins. Data downloaded can be directly related to surface measurements, for example, using a hyperspectral goniometer system,<sup>10,153–159</sup> which can measure the surface BRDF for validation purposes. However, to undertake a detailed analysis to understand these distributions would require the direct downlink of each frame in the pitchback maneuver necessitating significantly higher bandwidth.

#### 6. CONCLUSIONS

We have described an imaging spectrometer, an updated CCVIS design, which is uniquely suited to support the demanding requirements of aquatic ecosystem science as outlined in the CEOS performance standards. With its high SNR in the VNIR as well as the SWIR spectral ranges combined with excellent spatial resolution, this system will have a major impact on a variety of aquatic ecosystem applications in the coastal zone. Specifically, we have outlined how this system would improve the quantitative retrieval of critical aquatic ecosystem parameters in coastal wetlands and margins, corals, seagrasses and kelp, carbon cycling and sequestration in these systems, harmful algal blooms and hypoxia, as well as enable the modeling and monitoring of pollution, eutrophication, and water quality in coastal waters.

#### ACKNOWLEDGMENTS

The CCVIS was developed in collaboration with the NASA Earth Science and Technology Office under the direction of Parminder Ghuman and Keith Murray. Reference herein to any specific commercial product, process, or service by trade name, trademark, manufacturer, or otherwise, does not constitute or imply its endorsement by Lincoln Laboratory, Massachusetts Institute of Technology.

### REFERENCES

- [1] G. A. Maul and I. W. Duedall, *Demography of Coastal Populations*, pp. 692–700. Springer International Publishing, Cham, 2019.
- [2] G. A. Ballut-Dajud, L. C. Sandoval Herazo, G. Fernández-Lambert, J. L. Marín-Muñiz, M. C. López Méndez, and E. A. Betanzo-Torres, "Factors affecting wetland loss: A review," *Land* 11(3), p. 434, 2022.
- [3] M. Waycott, C. M. Duarte, T. J. Carruthers, R. J. Orth, W. C. Dennison, S. Olyarnik, A. Calladine, J. W. Fourqurean, K. L. Heck Jr, A. R. Hughes, et al., "Accelerating loss of seagrasses across the globe threatens coastal ecosystems," *Proceedings of the national academy of sciences* **106**(30), pp. 12377–12381, 2009.
- [4] K. B. Gedan, A. H. Altieri, and M. D. Bertness, "Uncertain future of new england salt marshes," *Marine Ecology Progress Series* **434**, pp. 229–237, 2011.
- [5] A. Rogers, J. L. Blanchard, and P. J. Mumby, "Vulnerability of coral reef fisheries to a loss of structural complexity," *Current Biology* **24**(9), pp. 1000–1005, 2014.
- [6] R. O. Green, A. Sen, J. C. Pearson, P. Mouroulis, S. Patel, P. Sullivan, T. Werne, M. Brenner, I. McKinley, E. Liggett, J. Rodriguez, M. Eastwood, S. T. Smith, E. Diaz, M. Bennett, R. Pollock, and M. Walch, "Surface biology and geology (sbg) visible to short wavelength infrared (vswir) wide swath instrument concept," in 2022 IEEE Aerospace Conference (AERO), pp. 1–10, IEEE, 2022.
- [7] "Thriving on our changing planet: A decadal strategy for earth observation from space," tech. rep., National Academies of Sciences, Engineering, and Medicine, 2018.
- [8] A. G. Dekker, N. Pinnel, P. Gege, X. Briottet, A. Court, S. Peters, K. R. Turpie, S. Sterckx, M. Costa, C. Giardino, V. E. Brando, F. Braga, M. Bergeron, T. Heege, and B. Pflug, "Feasibility study for an aquatic ecosystem earth observing system," ceos technical report, Committee on Earth Observation Satellites, 2018.
- [9] P. Gege and A. G. Dekker, "Spectral and radiometric measurement requirements for inland, coastal, and reef waters," *Remote Sensing* 12, p. 2247, 2020.

- [10] R. S. Eon and C. M. Bachmann, "Mapping barrier island soil moisture using a radiative transfer model of hyperspectral imagery from an unmanned aerial system," Scientific Reports 11(3270), 2021.
- [11] M. J. Montes, B.-C. Gao, and C. O. Davis, "NRL atmospheric correction algorithms for oceans: Tafkaa user's guide," tech. rep., NAVAL RESEARCH LAB WASHINGTON DC, 2004.
- [12] E. Mcleod, G. L. Chmura, S. Bouillon, R. Salm, M. Björk, C. M. Duarte, C. E. Lovelock, W. H. Schlesinger, and B. R. Silliman, "A blueprint for blue carbon: toward an improved understanding of the role of vegetated coastal habitats in sequestering co2," Frontiers in Ecology and the Environment 9(10), pp. 552–560, 2011.
- [13] J. Howard, S. Hoyt, K. Isensee, M. Telszewski, and E. Pidgeon, "Coastal blue carbon: methods for assessing carbon stocks and emissions factors in mangroves, tidal salt marshes, and seagrasses," 2014.
- [14] G. L. Chmura, S. C. Anisfeld, D. R. Cahoon, and J. C. Lynch, "Global carbon sequestration in tidal, saline wetland soils," *Global biogeochemical cycles* 17(4), 2003.
- [15] S. B. Goldsmith, C. S. Lapszynski, G. P. Badura, D. T. Osgood, C. M. Bachmann, and A. C. Tyler, "Assessing salt marsh vulnerability using high-resolution hyperspectral imagery," *Remote Sensing* 12(18), p. 2938, 2020.
- [16] X. Zhao, V. H. Rivera-Monroy, C. Li, I. V. Lopez, R. V. Rohli, Z. G. Xue, E. C. neda Moya, and C. Coronado-Molina, "Temperature across vegetation canopy-water-soil interfaces is modulated by hydroperiod and extreme weather in coastal wetlands," Frontiers in Marine Science, section Coastal Ocean Processes 9(852901), 2022.
- [17] C. Li, W. Huang, C. Chen, and H. Lin, "Flow regimes and adjustment to wind-driven motions in lake pontchartrain estuary: A modeling experiment using fvcom," *Journal of Geophysical Research: Oceans* 123(852901), 2018.
- [18] K. B. Byrd, J. L. O'Connell, S. Di Tommaso, and M. Kelly, "Evaluation of sensor types and environmental controls on mapping biomass of coastal marsh emergent vegetation," *Remote Sensing of Environment* 149, pp. 166–180, 2014.
- [19] M. S. Kearney, D. Stutzer, K. Turpie, and J. C. Stevenson, "The effects of tidal inundation on the reflectance characteristics of coastal marsh vegetation," *Journal of Coastal Research* 25(6), pp. 1177–1186, 2009.
- [20] J. Wang, Z. Liu, H. Yu, and F. Li, "Mapping spartina alterniflora biomass using lidar and hyperspectral data," Remote Sensing 9(6), p. 589, 2017.
- [21] H. Cheng, J. Wang, Y. Du, T. Zhai, Y. Fang, and Z. Li, "Exploring the potential of canopy reflectance spectra for estimating organic carbon content of aboveground vegetation in coastal wetlands," *International Journal of Remote Sensing* 42(10), pp. 3850–3872, 2021.
- [22] C. Zhang, S. Denka, H. Cooper, and D. R. Mishra, "Quantification of sawgrass marsh aboveground biomass in the coastal everglades using object-based ensemble analysis and landsat data," Remote Sensing of Environment 204, pp. 366–379, 2018.
- [23] Y. Mo, M. S. Kearney, J. A. Riter, F. Zhao, and D. R. Tilley, "Assessing biomass of diverse coastal marsh ecosystems using statistical and machine learning models," *International journal of applied earth observation and geoinformation* **68**, pp. 189–201, 2018.
- [24] R. S. Eon, S. Goldsmith, C. M. Bachmann, A. C. Tyler, C. S. Lapszynski, G. P. Badura, D. T. Osgood, and R. Brett, "Retrieval of salt marsh above-ground biomass from high-spatial resolution, multi-view hyperspectral imagery using PROSAIL," Remote Sensing 11, 2019.
- [25] H. Yang and J. Li, "Predictions of soil organic carbon using laboratory-based hyperspectral data in the northern tianshan mountains, china," *Environmental monitoring and assessment* 185(5), pp. 3897–3908, 2013.
- [26] N. B. Nur, K. Union, A. Miller, C. M. Bachmann, and A. C. Tyler, "Retrieval of soil organic carbon from hyperspectral imagery," in *AGU Fall Meeting 2022*, AGU, 2022 (Vol. 2022, pp. GC35A-03).
- [27] K. H. Mann, Ecology of coastal waters: with implications for management, John Wiley & Sons, 2009.
- [28] R. J. Miller, K. D. Lafferty, T. Lamy, L. Kui, A. Rassweiler, and D. C. Reed, "Giant kelp, macrocystis pyrifera, increases faunal diversity through physical engineering," *Proceedings of the Royal Society B: Biological Sciences* 285(1874), p. 20172571, 2018.
- [29] D. R. Schiel and M. S. Foster, The biology and ecology of giant kelp forests, Univ of California Press, 2015.

- [30] T. W. Bell, K. C. Cavanaugh, D. C. Reed, and D. A. Siegel, "Geographical variability in the controls of giant kelp biomass dynamics," *Journal of Biogeography* **42**(10), pp. 2010–2021, 2015.
- [31] T. Wernberg, D. A. Smale, F. Tuya, M. S. Thomsen, T. J. Langlois, T. De Bettignies, S. Bennett, and C. S. Rousseaux, "An extreme climatic event alters marine ecosystem structure in a global biodiversity hotspot," *Nature Climate Change* 3(1), pp. 78–82, 2013.
- [32] K. C. Cavanaugh, D. C. Reed, T. W. Bell, M. C. Castorani, and R. Beas-Luna, "Spatial variability in the resistance and resilience of giant kelp in southern and baja california to a multiyear heatwave," Frontiers in Marine Science 6, p. 413, 2019.
- [33] M. L. McPherson, D. J. Finger, H. F. Houskeeper, T. W. Bell, M. H. Carr, L. Rogers-Bennett, and R. M. Kudela, "Large-scale shift in the structure of a kelp forest ecosystem co-occurs with an epizootic and marine heatwave," *Communications biology* 4(1), pp. 1–9, 2021.
- [34] L. Rogers-Bennett and C. Catton, "Marine heat wave and multiple stressors tip bull kelp forest to sea urchin barrens," *Scientific reports* **9**(1), pp. 1–9, 2019.
- [35] T. W. Bell, J. G. Allen, K. C. Cavanaugh, and D. A. Siegel, "Three decades of variability in california's giant kelp forests from the landsat satellites," *Remote Sensing of Environment* 238, p. 110811, 2020.
- [36] T. W. Bell, K. C. Cavanaugh, and D. A. Siegel, "Remote monitoring of giant kelp biomass and physiological condition: An evaluation of the potential for the hyperspectral infrared imager (hyspiri) mission," Remote Sensing of Environment 167, pp. 218–228, 2015.
- [37] T. W. Bell, D. C. Reed, N. B. Nelson, and D. A. Siegel, "Regional patterns of physiological condition determine giant kelp net primary production dynamics," *Limnology and Oceanography* 63(1), pp. 472–483, 2018.
- [38] T. W. Bell and D. A. Siegel, "Nutrient availability and senescence spatially structure the dynamics of a foundation species," *Proceedings of the National Academy of Sciences* **119**(1), p. e2105135118, 2022.
- [39] S. Enríquez and N. Schubert, "Direct contribution of the seagrass thalassia testudinum to lime mud production," *Nature communications* **5**(1), pp. 1–12, 2014.
- [40] F. T. Short and S. Wyllie-Echeverria, "Natural and human-induced disturbance of seagrasses," Environmental conservation 23(1), pp. 17–27, 1996.
- [41] V. J. Hill, R. C. Zimmerman, W. P. Bissett, H. Dierssen, and D. D. Kohler, "Evaluating light availability, seagrass biomass, and productivity using hyperspectral airborne remote sensing in saint joseph's bay, florida," *Estuaries and coasts* **37**(6), pp. 1467–1489, 2014.
- [42] S. Phinn, C. Roelfsema, A. Dekker, V. Brando, and J. Anstee, "Mapping seagrass species, cover and biomass in shallow waters: An assessment of satellite multi-spectral and airborne hyper-spectral imaging systems in moreton bay (australia)," *Remote sensing of Environment* 112(8), pp. 3413–3425, 2008.
- [43] C. A. Carlson and D. A. Hansell, "Dom sources, sinks, reactivity, and budgets," *Biogeochemistry of marine dissolved organic matter*, pp. 65–126, 2015.
- [44] K. Mopper, D. J. Kieber, and A. Stubbins, "Marine photochemistry of organic matter: processes and impacts," *Biogeochemistry of marine dissolved organic matter*, pp. 389–450, 2015.
- [45] R. G. Najjar, M. Herrmann, R. Alexander, E. W. Boyer, D. Burdige, D. Butman, W.-J. Cai, E. A. Canuel, R. F. Chen, M. A. Friedrichs, et al., "Carbon budget of tidal wetlands, estuaries, and shelf waters of eastern north america," Global Biogeochemical Cycles 32(3), pp. 389–416, 2018.
- [46] T. J. Battin, L. A. Kaplan, S. Findlay, C. S. Hopkinson, E. Marti, A. I. Packman, J. D. Newbold, and F. Sabater, "Biophysical controls on organic carbon fluxes in fluvial networks," *Nature geoscience* 1(2), pp. 95–100, 2008.
- [47] L. Tranvik, J. J. Cole, and Y. T. Prairie, "The study of carbon in inland waters-from isolated ecosystems to players in the global carbon cycle," *Limnology and Oceanography letters* **3**(3), pp. 41–48, 2018.
- [48] N. Catalán, R. Marcé, D. N. Kothawala, L. Tranvik, et al., "Organic carbon decomposition rates controlled by water retention time across inland waters," Nature Geoscience 9(7), pp. 501–504, 2016.
- [49] M. Dai, Z. Yin, F. Meng, Q. Liu, and W.-J. Cai, "Spatial distribution of riverine doc inputs to the ocean: an updated global synthesis," *Current Opinion in Environmental Sustainability* 4(2), pp. 170–178, 2012.
- [50] C. Fabre, S. Sauvage, J.-L. Probst, and J. M. Sanchez-Pérez, "Global-scale daily riverine doc fluxes from lands to the oceans with a generic model," *Global and Planetary Change* **194**, p. 103294, 2020.

- [51] M. Meybeck, "Carbon, nitrogen, and phosphorus transport by world rivers," Am. J. Sci 282(4), pp. 401–450, 1982.
- [52] A. Menendez, M. Tzortziou, P. Neale, P. Megonigal, L. Powers, P. Schmitt-Kopplin, and M. Gonsior, "Strong dynamics in tidal marsh doc export in response to natural cycles and episodic events from continuous monitoring," *Journal of Geophysical Research: Biogeosciences* 127(7), p. e2022JG006863, 2022.
- [53] D. L. Childers, J. W. Day, and H. N. Mckellar, "Twenty more years of marsh and estuarine flux studies: revisiting nixon (1980)," *Concepts and controversies in tidal marsh ecology*, pp. 391–423, 2002.
- [54] H. N. Schiebel, G. B. Gardner, X. Wang, F. Peri, and R. F. Chen, "Seasonal export of dissolved organic matter from a new england salt marsh," *Journal of Coastal Research* 34(4), pp. 939–954, 2018.
- [55] J. I. Hedges, R. G. Keil, and R. Benner, "What happens to terrestrial organic matter in the ocean?," Organic geochemistry 27(5-6), pp. 195–212, 1997.
- [56] W.-J. Cai, "Estuarine and coastal ocean carbon paradox: Co2 sinks or sites of terrestrial carbon incineration?," *Annual review of marine science* **3**, pp. 123–145, 2011.
- [57] J.-P. Gattuso, M. Frankignoulle, and R. Wollast, "Carbon and carbonate metabolism in coastal aquatic ecosystems," Annual Review of Ecology and Systematics, pp. 405–434, 1998.
- [58] D. A. Hansell, C. A. Carlson, D. J. Repeta, and R. Schlitzer, "Dissolved organic matter in the ocean: A controversy stimulates new insights," *Oceanography* **22**(4), pp. 202–211, 2009.
- [59] F. Azam, D. Smith, G. Steward, and Å. Hagström, "Bacteria-organic matter coupling and its significance for oceanic carbon cycling," *Microbial ecology* 28(2), pp. 167–179, 1994.
- [60] T. R. Anderson and H. W. Ducklow, "Microbial loop carbon cycling in ocean environments studied using a simple steady-state model," *Aquatic Microbial Ecology* **26**(1), pp. 37–49, 2001.
- [61] C. Freeman, N. Fenner, N. Ostle, H. Kang, D. Dowrick, B. Reynolds, M. Lock, D. Sleep, S. Hughes, and J. Hudson, "Export of dissolved organic carbon from peatlands under elevated carbon dioxide levels," *Nature* 430(6996), pp. 195–198, 2004.
- [62] C. Lønborg, C. Carreira, T. Jickells, and X. A. Álvarez-Salgado, "Impacts of global change on ocean dissolved organic carbon (doc) cycling," Frontiers in Marine Science 7, p. 466, 2020.
- [63] D. T. Monteith, J. L. Stoddard, C. D. Evans, H. A. De Wit, M. Forsius, T. Høgåsen, A. Wilander, B. L. Skjelkvåle, D. S. Jeffries, J. Vuorenmaa, et al., "Dissolved organic carbon trends resulting from changes in atmospheric deposition chemistry," Nature 450(7169), pp. 537–540, 2007.
- [64] P. Regnier, P. Friedlingstein, P. Ciais, F. T. Mackenzie, N. Gruber, I. A. Janssens, G. G. Laruelle, R. Lauerwald, S. Luyssaert, A. J. Andersson, et al., "Anthropogenic perturbation of the carbon fluxes from land to ocean," Nature geoscience 6(8), pp. 597–607, 2013.
- [65] S. Moore, C. D. Evans, S. E. Page, M. H. Garnett, T. G. Jones, C. Freeman, A. Hooijer, A. J. Wiltshire, S. H. Limin, and V. Gauci, "Deep instability of deforested tropical peatlands revealed by fluvial organic carbon fluxes," *Nature* 493(7434), pp. 660–663, 2013.
- [66] A. G. Hounshell, J. C. Rudolph, B. R. Van Dam, N. S. Hall, C. L. Osburn, and H. W. Paerl, "Extreme weather events modulate processing and export of dissolved organic carbon in the neuse river estuary, nc," Estuarine, Coastal and Shelf Science 219, pp. 189–200, 2019.
- [67] F. E. Muller-Karger, E. Hestir, C. Ade, K. Turpie, D. A. Roberts, D. Siegel, R. J. Miller, D. Humm, N. Izenberg, M. Keller, et al., "Satellite sensor requirements for monitoring essential biodiversity variables of coastal ecosystems," Ecological applications 28(3), pp. 749–760, 2018.
- [68] F. Cao and M. Tzortziou, "Capturing dissolved organic carbon dynamics with landsat-8 and sentinel-2 in tidally influenced wetland–estuarine systems," *Science of the Total Environment* 777, p. 145910, 2021.
- [69] O. Cronin-Golomb, J. P. Harringmeyer, M. W. Weiser, X. Zhu, N. Ghosh, A. B. Novak, I. Forbrich, and C. G. Fichot, "Modeling benthic solar exposure (uv and visible) in dynamic coastal systems to better inform seagrass habitat suitability," *Science of The Total Environment* 812, p. 151481, 2022.
- [70] C. L. Osburn, M. P. Mikan, J. R. Etheridge, M. R. Burchell, and F. Birgand, "Seasonal variation in the quality of dissolved and particulate organic matter exchanged between a salt marsh and its adjacent estuary," *Journal of Geophysical Research: Biogeosciences* 120(7), pp. 1430–1449, 2015.

- [71] I. D. Joshi, E. J. D'Sa, C. L. Osburn, T. S. Bianchi, D. S. Ko, D. Oviedo-Vargas, A. R. Arellano, and N. D. Ward, "Assessing chromophoric dissolved organic matter (cdom) distribution, stocks, and fluxes in apalachicola bay using combined field, viirs ocean color, and model observations," Remote sensing of environment 191, pp. 359–372, 2017.
- [72] P. A. Raymond and J. E. Saiers, "Event controlled doc export from forested watersheds," Biogeochemistry 100(1), pp. 197–209, 2010.
- [73] R. M. Holmes, J. W. McClelland, P. A. Raymond, B. B. Frazer, B. J. Peterson, and M. Stieglitz, "Lability of doc transported by alaskan rivers to the arctic ocean," *Geophysical Research Letters* 35(3), 2008.
- [74] G. M. Silsbe, M. J. Behrenfeld, K. H. Halsey, A. J. Milligan, and T. K. Westberry, "The cafe model: A net production model for global ocean phytoplankton," *Global Biogeochemical Cycles* 30(12), pp. 1756–1777, 2016.
- [75] C. G. Fichot and W. L. Miller, "An approach to quantify depth-resolved marine photochemical fluxes using remote sensing: Application to carbon monoxide (co) photoproduction," Remote Sensing of Environment 114(7), pp. 1363–1377, 2010.
- [76] S. V. Smith, "Coral-reef area and contributions of reefs to processes and resources of the world's oceans," *Nature* **273**(5659), pp. 225–226, 1978.
- [77] J. A. Kleypas, "Modeled estimates of global reef habitat and carbonate production since the last glacial maximum," *Paleoceanography* **12**(4), pp. 533–545, 1997.
- [78] M. D. Spalding and A. M. Grenfell, "New estimates of global and regional coral reef areas," *Coral Reefs* **16**(4), pp. 225–230, 1997.
- [79] R. Costanza, R. De Groot, P. Sutton, S. Van der Ploeg, S. J. Anderson, I. Kubiszewski, S. Farber, and R. K. Turner, "Changes in the global value of ecosystem services," *Global environmental change* 26, pp. 152–158, 2014.
- [80] F. Moberg and C. Folke, "Ecological goods and services of coral reef ecosystems," Ecological Economics 29(2), pp. 215–233, 1999.
- [81] T. J. Done, "Phase shifts in coral reef communities and their ecological significance," *Hydrobiologia* **247**(1/3), pp. 121–132, 1992.
- [82] T. J. Done, "Ecological criteria for evaluating coral reefs and their implications for managers and researchers," *Coral Reefs* **14**(4), pp. 183–192, 1995.
- [83] J. H. Connell, "Disturbance and recovery of coral assemblages," Coral Reefs 16(5), pp. S101–S113, 1997.
- [84] J. P. Gatusso, O. Hoegh-Guldberg, and H. O. Pörtner, Cross-chapter box on coral reefs, pp. 97–100. Cambridge University Press, Cambridge, United Kingdom and New York, NY, USA, 2014.
- [85] E. J. Hochberg and M. J. Atkinson, "Capabilities of remote sensors to classify coral, algae and sand as pure and mixed spectra," *Remote Sensing of Environment* 85(2), pp. 174–189, 2003.
- [86] D. R. Thompson, E. J. Hochberg, G. P. Asner, R. O. Green, D. E. Knapp, B.-C. Gao, R. Garcia, M. Gierach, Z. Lee, and S. Maritorena, "Airborne mapping of benthic reflectance spectra with bayesian linear mixtures," *Remote Sensing of Environment* 200, pp. 18–30, 2017.
- [87] S. B. Watson, C. Miller, G. Arhonditsis, G. L. Boyer, W. Carmichael, M. N. Charlton, R. Confesor, D. C. Depew, T. O. Höök, S. A. Ludsin, G. Matisoff, S. P. McElmurry, M. W. Murray, R. Peter Richards, Y. R. Rao, M. M. Steffen, and S. W. Wilhelm, "The re-eutrophication of lake erie: Harmful algal blooms and hypoxia," *Harmful Algae* 56, pp. 44–66, 2016.
- [88] D. M. Anderson, P. Hoagland, Y. Kaoru, and A. W. White, "Estimated annual economic impacts from harmful algal blooms (habs) in the united states," tech. rep., Woods Hole Oceanographic Institution, 2000. https://www.whoi.edu/cms/files/Economics\_report\_18564\_23050.pdf.
- [89] "Bureau of labor inflation calculator." https://www.bls.gov/data/inflation\_calculator.htm.
- [90] D. Breitburg, L. A. Levin, A. Oschlies, M. Grégoire, F. P. Chavez, D. J. Conley, V. Garçon, D. Gilbert, D. Gutiérrez, K. Isensee, G. S. Jacinto, K. E. Limburg, I. Montes, S. W. A. Naqvi, G. C. Pitcher, N. N. Rabalais, M. R. Roman, K. A. Rose, B. A. Seibel, M. Telszewski, M. Yasuhara, and J. Zhang, "Declining oxygen in the global ocean and coastal waters," *Science* 359(6371), p. eaam7240, 2018.

- [91] K. M. Purcell, J. K. Craig, J. M. Nance, M. D. Smith, and L. S. Bennear, "Fleet behavior is responsive to a large-scale environmental disturbance: Hypoxia effects on the spatial dynamics of the northern gulf of mexico shrimp fishery," *PloS one* 12(8), p. e0183032, 2017.
- [92] M. D. Smith, A. Oglend, A. J. Kirkpatrick, F. Asche, L. S. Bennear, J. K. Craig, and J. M. Nance, "Seafood prices reveal impacts of a major ecological disturbance," *Proceedings of the National Academy of Sciences* 114(7), pp. 1512–1517, 2017.
- [93] D. R. Obenour, D. Scavia, N. N. Rabalais, R. E. Turner, and A. M. Michalak, "Retrospective analysis of midsummer hypoxic area and volume in the northern gulf of mexico, 1985–2011," *Environmental science & technology* 47(17), pp. 9808–9815, 2013.
- [94] D. Scavia, J. D. Allan, K. K. Arend, S. Bartell, D. Beletsky, N. S. Bosch, S. B. Brandt, R. D. Briland, I. Daloğlu, J. V. DePinto, D. M. Dolan, M. A. Evans, T. M. Farmer, D. Goto, H. Hanm, T. O. Höök, R. Knight, S. A. Ludsin, D. Mason, A. M. Michalak, R. P. Richards, J. J. Roberts, D. K. Rucinski, E. Rutherford, D. J. Schwabt, T. M. Sesterhenn, H. Zhang, and Y. Zhou, "Assessing and addressing the re-eutrophication of lake erie: Central basin hypoxia," *Journal of Great Lakes Research* 40(2), pp. 226–246, 2014
- [95] N. N. Rabalais, R. E. Turner, and D. Scavia, "Beyond Science into Policy: Gulf of Mexico Hypoxia and the Mississippi River: Nutrient policy development for the Mississippi River watershed reflects the accumulated scientific evidence that the increase in nitrogen loading is the primary factor in the worsening of hypoxia in the northern Gulf of Mexico," BioScience 52, pp. 129–142, 02 2002.
- [96] R. E. Turner, N. N. Rabalais, and D. Justic, "Gulf of mexico hypoxia: Alternate states and a legacy," Environmental Science & Technology 42(7), pp. 2323–2327, 2008.
- [97] "Gcoos hab forecasting." https://gcoos.org/expanding-the-respiratory-forecast/.
- [98] L. Wang and D. Justić, "A modeling study of the physical processes affecting the development of seasonal hypoxia over the inner louisiana-texas shelf: Circulation and stratification," Continental Shelf Research 29(11), pp. 1464–1476, 2009.
- [99] M. N. Allahdadi, F. Jose, and C. Patin, "Seasonal Hydrodynamics along the Louisiana Coast: Implications for Hypoxia Spreading," *Journal of Coastal Research* **29**(5), pp. 1092 1100, 2013.
- [100] Y. Feng, K. Fennel, G. A. Jackson, S. F. DiMarco, and R. D. Hetland, "A model study of the response of hypoxia to upwelling-favorable wind on the northern gulf of mexico shelf," *Journal of Marine Systems* **131**, pp. 63–73, 2014.
- [101] J. K. Jolliff, E. Jarosz, S. Ladner, T. Smith, S. Anderson, and J. Dykes, "The optical signature of a bottom boundary layer ventilation event in the northern gulf of mexico's hypoxic zone," *Geophysical Research* Letters 45(16), pp. 8390–8398, 2018.
- [102] C. Hu, Z. Lee, R. Ma, K. Yu, D. Li, and S. Shang, "Moderate resolution imaging spectroradiometer (modis) observations of cyanobacteria blooms in taihu lake, china," *Journal of Geophysical Research: Oceans* 115(C4), 2010.
- [103] G. Wang, Z. Lee, D. R. Mishra, and R. Ma, "Retrieving absorption coefficients of multiple phytoplankton pigments from hyperspectral remote sensing reflectance measured over cyanobacteria bloom waters," *Limnology and Oceanography: Methods* 14(7), pp. 432–447, 2016.
- [104] T. J. Judice, E. A. Widder, W. H. Falls, D. M. Avouris, D. J. Cristiano, and J. D. Ortiz, "Field-validated detection of aureoumbra lagunensis brown tide blooms in the indian river lagoon, florida, using sentinel-3a olci and ground-based hyperspectral spectroradiometers," GeoHealth 4(6), p. e2019GH000238, 2020.
- [105] G. Wang, Z. Lee, and C. Mouw, "Multi-spectral remote sensing of phytoplankton pigment absorption properties in cyanobacteria bloom waters: A regional example in the western basin of lake erie," REMOTE SENSING 9, DEC 2017.
- [106] J. D. Ortiz, D. M. Avouris, S. J. Schiller, J. C. Luvall, J. D. Lekki, R. P. Tokars, R. C. Anderson, R. Shuchman, M. Sayers, and R. Becker, "Evaluating visible derivative spectroscopy by varimax-rotated, principal component analysis of aerial hyperspectral images from the western basin of lake erie," *Journal* of Great Lakes Research 45(3), pp. 522–535, 2019.
- [107] A. Vander Woude, S. Ruberg, T. Johengen, R. Miller, and D. Stuart, "Spatial and temporal scales of variability of cyanobacteria harmful algal blooms from noaa glerl airborne hyperspectral imagery," *Journal of Great Lakes Research* 45(3), pp. 536–546, 2019.

- [108] Y. S. Kwon, J. Pyo, Y.-H. Kwon, H. Duan, K. H. Cho, and Y. Park, "Drone-based hyperspectral remote sensing of cyanobacteria using vertical cumulative pigment concentration in a deep reservoir," Remote Sensing of Environment 236, p. 111517, 2020.
- [109] V. Chávez, A. Uribe-Martínez, E. Cuevas, R. E. Rodríguez-Martínez, B. I. van Tussenbroek, V. Francisco, M. Estévez, L. B. Celis, L. V. Monroy-Velázquez, R. Leal-Bautista, et al., "Massive influx of pelagic sargassum spp. on the coasts of the mexican caribbean 2014–2020: challenges and opportunities," Water 12(10), p. 2908, 2020.
- [110] J. Gower, C. Hu, G. Borstad, and S. King, "Ocean color satellites show extensive lines of floating sargassum in the gulf of mexico," *IEEE Transactions on Geoscience and Remote Sensing* **44**(12), pp. 3619–3625, 2006.
- [111] C. R. Anderson, E. Berdalet, R. M. Kudela, C. K. Cusack, J. Silke, E. O'Rourke, D. Dugan, M. McCammon, J. A. Newton, S. K. Moore, et al., "Scaling up from regional case studies to a global harmful algal bloom observing system," Frontiers in Marine Science, p. 250, 2019.
- [112] F. Antonio-Martínez, Y. Henaut, A. Vega-Zepeda, A. I. Cerón-Flores, R. Raigoza-Figueras, N. P. Cetz-Navarro, and J. Espinoza-Avalos, "Leachate effects of pelagic sargassum spp. on larval swimming behavior of the coral acropora palmata," *Scientific reports* **10**(1), pp. 1–13, 2020.
- [113] B. I. Van Tussenbroek, H. A. H. Arana, R. E. Rodríguez-Martínez, J. Espinoza-Avalos, H. M. Canizales-Flores, C. E. González-Godoy, M. G. Barba-Santos, A. Vega-Zepeda, and L. Collado-Vides, "Severe impacts of brown tides caused by sargassum spp. on near-shore caribbean seagrass communities," *Marine pollution bulletin* 122(1-2), pp. 272–281, 2017.
- [114] A. Williams and R. A. Feagin, "Sargassum and beach erosion: Potential costs and benefits for coastal managers," 2010.
- [115] C. Hu, "A novel ocean color index to detect floating algae in the global oceans," Remote Sensing of Environment 113(10), pp. 2118–2129, 2009.
- [116] C. Hu, L. Feng, R. F. Hardy, and E. J. Hochberg, "Spectral and spatial requirements of remote measurements of pelagic sargassum macroalgae," *Remote Sensing of Environment* 167, pp. 229–246, 2015.
- [117] T. T. Wynne, R. P. Stumpf, M. C. Tomlinson, R. Warner, P. A. Tester, J. Dyble, and G. L. Fahnenstiel, "Relating spectral shape to cyanobacterial blooms in the laurentian great lakes," *International Journal of Remote Sensing* 29(12), pp. 3665–3672, 2008.
- [118] T. T. Wynne, R. P. Stumpf, M. C. Tomlinson, and J. Dyble, "Characterizing a cyanobacterial bloom in western lake erie using satellite imagery and meteorological data," *Limnology and Oceanography* 55(5), pp. 2025–2036, 2010.
- [119] T. T. Wynne and R. P. Stumpf, "Spatial and temporal patterns in the seasonal distribution of toxic cyanobacteria in western lake eric from 2002–2014," *Toxins* **7**(5), pp. 1649–1663, 2015.
- [120] R. T. Ford and A. Vodacek, "Determining improvements in landsat spectral sampling for inland water quality monitoring," *Science of Remote Sensing* 1, p. 100005, 2020.
- [121] R. Ford, Water Quality and Algal Bloom Sensing from Multiple Imaging Platforms. PhD thesis, Rochester Institute of Technology, Center for Imaging Science, 2019.
- [122] C. D. Mobley, Light and Water: Radiative Transfer in Natural Waters, Academic press, 1994.
- [123] C. D. Mobley and L. K. Sundman, "Hydrolight 5 ecolight 5," Sequoia Scientific Inc., p. 16, 2008.
- [124] C. D. Mobley, L. K. Sundman, C. O. Davis, J. H. Bowles, T. V. Downes, R. A. Leathers, M. J. Montes, W. P. Bissett, D. D. Kohler, R. P. Reid, E. M. Louchard, and A. Gleason, "Interpretation of hyperspectral remote-sensing imagery by spectrum matching and look-up tables," *Applied Optics* 44(17), pp. 3576–3592, 2005.
- [125] J. A. Concha and J. R. Schott, "Retrieval of color producing agents in case 2 waters using landsat 8," Remote Sensing of Environment 185, pp. 95–107, 2016.
- [126] J. A. Concha, The Use of Landsat 8 for Monitoring of Fresh and Coastal Waters. PhD thesis, Rochester Institute of Technology, Center for Imaging Science, 2015.
- [127] J. A. Curcio and C. C. Petty, "The near infrared absorption spectrum of liquid water," *JOSA* 41(5), pp. 302–304, 1951.
- [128] B.-C. Gao, K. B. Heidebrecht, and A. F. Goetz, "Derivation of scaled surface reflectances from aviris data," Remote Sensing of Environment 44(2), pp. 165–178, 1993.

- [129] B.-C. Gao, M. J. Montes, Z. Ahmad, and C. O. Davis, "Atmospheric correction algorithm for hyperspectral remote sensing of ocean color from space," *Applied Optics* **39**(6), pp. 887–896, 2000.
- [130] H. R. Gordon and M. Wang, "Retrieval of water-leaving radiance and aerosol optical thickness over the oceans with seawifs: a preliminary algorithm," *Appl. Opt.* **33**(3), pp. 443–452, 1994.
- [131] L. Gross-Colzy, S. Colzy, R. Frouin, and P. Henry, "A general ocean color atmospheric correction scheme based on principal components analysis: Part i. performance on case 1 and case 2 waters," in *Coastal Ocean Remote Sensing*, **6680**, pp. 9–20, SPIE, 2007.
- [132] R. J. Frouin, B. A. Franz, A. Ibrahim, K. Knobelspiesse, Z. Ahmad, B. Cairns, J. Chowdhary, H. M. Dierssen, J. Tan, O. Dubovik, et al., "Atmospheric correction of satellite ocean-color imagery during the pace era," Frontiers in earth science 7, p. 145, 2019.
- [133] ARTDECO code web site. https://www.icare.univ-lille.fr/artdeco/.
- [134] C. D. Mobley, "A numerical model for the computation of radiance distributions in natural waters with wind-roughened surfaces," *Limnology and oceanography* **34**(8), pp. 1473–1483, 1989.
- [135] R. Santer and C. Schmechtig, "Adjacency effects on water surfaces: primary scattering approximation and sensitivity study," *Applied optics* **39**(3), pp. 361–375, 2000.
- [136] A. Girard and P. Jacquinot, "Principles of instrumental methods in spectroscopy," in Advanced Optical Techniques, A. C. S. V. Heel, ed., Wiley Series in Pure and Applied Optics, ch. 3, pp. 73–121, North-Holland Publishing Company, 1967.
- [137] B. V. Gorp, P. Mouroulis, D. W. Wilson, and R. O. Green, "Design of the Compact Wide Swath Imaging Spectrometer (CWIS)," *Proceedings of SPIE* **9222**, pp. 92220C1–9, SPIE, 2014.
- [138] P. Mouroulis, R. O. Green, and T. G. Chrien, "Design of pushbroom imaging spectrometers for optimum recovery of spectroscopic and spatial information," *Applied Optics* **39**(13), pp. 2210–2220, 2000.
- [139] M. P. Chrisp, R. B. Lockwood, M. A. Smith, G. Balonek, C. Holtsberg, K. J. Thome, K. E. Murray, and P. Ghuman, "Development of a compact imaging spectrometer form for the solar reflective spectral region," *Applied Optics* **59**(32), pp. 10007–10017, 2020.
- [140] M. A. Smith, S. Berry, L. Parameswaran, C. Holtsberg, N. Siegel, R. Lockwood, M. P. Chrisp, D. Freeman, and M. Rothschild, "Design, simulation, and fabrication of three-dimensional microsystem components using grayscale photolithography," *Journal of Micro/Nanolithography, MEMS, and MOEMS* 18(04), pp. 043507–1-043507–13, 2019.
- [141] P. Jerram and J. Beletic, "Teledyne's high performance infrared detectors for space missions," *Proceedings* of SPIE 11180, pp. 111803D-1-111803D-10, SPIE, 2018.
- [142] T. Scientific and Imaging, "Geosnap-18 focal plane array." Accessed on April 4, 2023.
- [143] D. J. Diner, J. C. Beckert, T. H. Reilly, C. J. Bruegge, J. E. Conel, R. A. Kahn, J. V. Martonchik, T. P. Ackerman, R. Davies, S. A. Gerstl, et al., "Multi-angle imaging spectroradiometer (misr) instrument description and experiment overview," *IEEE Transactions on Geoscience and Remote Sensing* 36(4), pp. 1072–1087, 1998.
- [144] R. Kahn, P. Banerjee, and D. McDonald, "Sensitivity of multiangle imaging to natural mixtures of aerosols over ocean," *Journal of Geophysical Research: Atmospheres* **106**(D16), pp. 18219–18238, 2001.
- [145] R. A. Kahn, B. J. Gaitley, M. J. Garay, D. J. Diner, T. F. Eck, A. Smirnov, and B. N. Holben, "Multiangle imaging spectroradiometer global aerosol product assessment by comparison with the aerosol robotic network," *Journal of Geophysical Research: Atmospheres* 115(D23), 2010.
- [146] R. A. Kahn and B. J. Gaitley, "An analysis of global aerosol type as retrieved by misr," *Journal of Geophysical Research: Atmospheres* **120**(9), pp. 4248–4281, 2015.
- [147] P. deSouza, R. A. Kahn, J. A. Limbacher, E. A. Marais, F. Duarte, and C. Ratti, "Combining low-cost, surface-based aerosol monitors with size-resolved satellite data for air quality applications," *Atmospheric Measurement Techniques* **13**(10), pp. 5319–5334, 2020.
- [148] T. He, S. Liang, and D. Wang, "Direct estimation of land surface albedo from simultaneous misr data," *IEEE Transactions on Geoscience and Remote Sensing* **55**(5), pp. 2605–2617, 2017.
- [149] J. D. Armston, P. F. Scarth, S. R. Phinn, and T. J. Danaher, "Analysis of multi-date misr measurements for forest and woodland communities, queensland, australia," *Remote Sensing of Environment* **107**(1-2), pp. 287–298, 2007.

- [150] Z. Han, T. Cheng, X. Gu, S. Shi, X. Li, and K. Bi, "A multi-angle method for simultaneous retrieval of aerosol optical depth and bidirectional reflectance over case ii waters," Frontiers in Environmental Science , p. 664, 2022.
- [151] R. S. Eon, C. M. Bachmann, C. S. Lapszynski, A. C. Tyler, and S. Goldsmith, "Retrieval of sediment filling factor in a salt panne from multi-view hyperspectral imagery," *Remote Sensing* 12(3), p. 422, 2020.
- [152] R. S. Eon, C. M. Bachmann, and A. D. Gerace, "Retrieval of sediment fill factor by inversion of a modified hapke model applied to sampled herf from airborne and satellite imagery," *Remote Sensing* **10**(11), p. 1758, 2018.
- [153] J. D. Harms, C. M. Bachmann, B. L. Ambeau, J. W. Faulring, A. J. R. Torres, G. Badura, and E. Myers, "Fully automated laboratory and field-portable goniometer used for performing accurate and precise multiangular reflectance measurements," *Journal of Applied Remote Sensing* 11(4), pp. 046014–15, 2017.
- [154] C. M. Bachmann, R. S. Eon, B. Ambeau, J. Harms, G. Badura, and C. Griffo, "Modeling and intercomparison of field and laboratory hyperspectral goniometer measurements with g-liht imagery of the algodones dunes," *Journal of Applied Remote Sensing* 12(1), p. 012005, 2017.
- [155] J. McCorkel, C. M. Bachmann, C. Coburn, A. D. Gerace, L. Leigh, J. S. Czapla-Myers, D. L. Helder, and B. D. Cook, "Overview of the 2015 algodones sand dunes field campaign to support sensor intercalibration," *Journal of Applied Remote Sensing* 12(1), p. 012003, 2017.
- [156] G. Badura and C. M. Bachmann, "Assessing effects of azimuthally oriented roughness on directional reflectance of sand," *IEEE Journal of Selected Topics in Applied Earth Observations and Remote Sens*ing 12(3), pp. 1012–1025, 2019.
- [157] G. Badura, C. M. Bachmann, J. Harms, and A. Abelev, "Observed relationship between brf spectral-continuum variance and macroscopic roughness of clay sediments," *IEEE Transactions on Geoscience and Remote Sensing* **57**(9), pp. 6726–6740, 2019.
- [158] D. J. Shiltz and C. M. Bachmann, "An alternative to hapke's macroscopic roughness correction," Icarus 390, p. 115240, 2023.
- [159] N. B. Nur and C. M. Bachmann, "Comparison of soil moisture content retrieval models utilizing hyperspectral goniometer data and hyperspectral imagery from an unmanned aerial system," *Journal of Geophysical Research: Biogeosciences* 128, p. e2023JG007381, 2023.